

High-Resolution Optical Imaging from Trajectory Time Distributions

Erwen Mei and Robin M. Hochstrasser*

Chemistry Department, University of Pennsylvania, Philadelphia, Pennsylvania 19104

Received: August 9, 2006; In Final Form: October 4, 2006

Trajectory time distribution optical microscopy (TTDOM), which records the mean off-times of single molecular fluorescent indicators that light up when they collide with vesicles, is extended to record fluorescence durations or on-times. TTDOM can distinguish shapes of objects that are smaller than the diffraction limited resolution. The fluorescence duration time image can also provide high-resolution information. The effects of the threshold that separates fluorescent bursts from background signals and of two or more probes visiting the vesicles simultaneously have been investigated systematically. New experimental results along with simulations indicate that TTDOM is capable of providing the size and shape of objects and information on probe-vesicle binding.

Introduction

The resolution of optical microscopes is limited by the wavelength, the numerical aperture (N.A.) of the objective, and the sample environments, which perturb the penetrating path of the light through the sample.¹ It is of great interest to develop methods that do not have these limitations. One subdiffraction limit approach is near field scanning optical microscopy (NSOM), in which a near field probe is used to restrict the size of the light source to the subwavelength range.^{2,3} The high resolution is achieved if the NSOM probe is placed close enough to the specimen. The resolution reported for NSOM ranges from 100 nm down to a few nanometers.^{4,5} This scanning tip method has proven very valuable and progress in tip manufacture and understanding sample-tip interactions will further widen the scope of the method. A 4Pi-confocal microscope and a microscope with reversible saturable optical fluorescence transitions (RESOLET) between two states as well as one based on stimulated emission are other approaches to obtain subdiffraction optical images.^{6–8} In 4Pi-microscopy, the resolution is improved by using two objectives, which increase the N.A. by doubling the collecting cone angle. In RESOLET microscope, to achieve high resolution beyond the diffraction limit, two lasers are used to switch the fluorophores between two states, usually between an emissive and a dark state.⁸ In the microscope based on stimulated emission, the size of the focused laser beam is significantly reduced by overlapping it with a second infrared laser. Recently, high-resolution images of single molecules have been obtained by means of a low noise high quantum yield CCD that records fluorescence images of individual molecules.^{9–12} Two identical fluorophores in the *xy*-plane separated by distances as small as ~ 10 nm have been resolved by this method, which provides an effective way to measure the distance ranging from a few nanometers to 200 nm between two fluorescent molecules. There remain challenges in the control of the photobleaching of groups of molecules and hence the separations among them. A subdiffraction-limited optical imaging method has also been demonstrated recently by using a silver superlens, which allows the recovery of evanescent waves in an image.¹³

Recently, a new high-resolution microscopy we call trajectory time distribution optical microscopy (TTDOM) has been

demonstrated.¹⁴ Instead of measuring light intensity for imaging TTDOM measures the fluorescence statistics of single molecular probes or beacons, colliding with an object/or objects of interest. One such beacon is Nile Red (NR), which has negligible fluorescence in water, but emits strong fluorescence when it associates with hydrophobic lipid vesicles.¹⁵ The frequency of fluorescence bursts (the fluorescence off rate) is proportional to the collision rate of freely diffusing NR molecules with an immobilized vesicle,¹⁵ which is approximately given by $2\pi DNR$, where D is the diffusion coefficient, N is the number density of NR, and R the radius of a surface immobilized vesicle having a hemispherical shape. Recording the mean of the fluorescence off-rate as a function of the location of an object in the *xy*-plane provides a high-resolution optical image that is not limited by diffraction. Furthermore, with the knowledge of D and N , values of R smaller than optical resolution can be directly obtained from the fluorescence off-rate image.

Here, we extend TTDOM to record both the mean values of the fluorescence off-rates and the on-times. We show that both these measurements allow high-resolution imaging. The effect of the threshold that is used to separate fluorescence signals from the background signals in calculating off-times and on-times has also been investigated quantitatively in this report. The capability of TTDOM to distinguish nanoscale objects having different shapes has been demonstrated by the simulations.

Materials and Methods

The Microscope. The scanning confocal microscope, described previously,¹⁶ uses a scanning stage (Queensgate), with closed-loop X, Y feedback for accurate sample positioning and location of individual molecules, that is controlled by a modified Nanoscope E Controller (Digital Instruments). The sample and stage were mounted on an inverted, epi-illumination microscope (Nikon, Diaphot 300). The 514.5 nm argon line was circularly polarized and used for excitation at a power of ~ 30 μ W. A Nikon FLUOR X40, 1.3 numerical aperture objective was used to produce a nearly diffraction-limited focus on the sample and to collect the fluorescence. Appropriate combinations of notch (Kaiser Optical), band-pass, long-pass, and dichroic filters (Chroma Technology) were used to spectrally isolate the fluorescence peaked at 630 nm: the detector was a single-photon

* Address correspondence to this author.

counting avalanche diode. The fluorescence spectra from single vesicles were checked by means of a monochromator (Acton Research) equipped with a back-illumination liquid-nitrogen-cooled CCD camera (Princeton Instruments, Trenton, NJ).

Materials. The fluorescent probe NR, which we often refer to as the beacon, was purchased from Molecular Probes and used as received. Glass coverslips and cylinders (Fisher) were cleaned by sequential sonication in 2 M sodium hydroxide solution, methanol, 2 M sodium hydroxide solution, and DI water. The 1,2-dimyristoyl-*sn*-glycero-3-phosphocholine (DMPC) (Avanti Polar Lipids) was used to prepare large unilamellar vesicles (LUVs) as follows:¹⁷ 0.25 mL of 25 mg/mL DMPC lipids in CHCl_3 was evaporated in nitrogen to yield a dry phospholipids film on the internal surface of a vial. After 2 h in vacuum the lipid film was hydrated in 4 mL of phosphate buffer (20 mM, pH 7.0) with vigorous stirring at 32 °C for 1.5 h. The resulting vesicles were subjected to 5 freeze/thaw cycles and extruded about 20 times through polycarbonate membranes having 100 nm pore diameter (Avanti Mini-Extruder) and used within 2 days. The concentration used in the single vesicle experiment is ~ 1 pM at which the individual ~ 50 nm radius vesicles adsorbed on the glass surface have a mean nearest neighbor separation of ~ 1.5 μm .¹⁷

The lipid DMPC has a phase transition temperature of ~ 23 °C and at the temperature of the experiments the ordered gel and disordered liquid crystalline phase coexist.^{18,19} Previous AFM work has shown that LUVs flatten considerably upon adsorption to glass and mica surfaces^{20,21} and that they stick on glass and mica surfaces as intact vesicles, partially broken vesicles, and lipid bilayer disks depending on their size. Vesicles having mean diameters between 30 and 100 nm are mostly intact.²⁰ Some of the vesicles that move very slowly were not reported in this work. Our experiments, based on the detection of the fluorescence of single NR molecules bound to the lipid bilayers, could not directly establish structure differences among these membranes because the vesicle–NR interaction is not fully understood. The observed heterogeneity for DMPC vesicles is certainly influenced by the glass surface.^{18,22} The majority of the fluorescence burst width distributions associated with immobilized single DMPC vesicles exhibited a single-exponential decay of NR fluorescence so most of the vesicles act like single structure domains.¹⁵

Results and Discussion

Figure 1a shows a fluorescence image of surface immobilized DMPC vesicles in a buffer containing freely diffusing NR molecules. Such an image is observed only when both NR molecules and vesicles exist in the system. Figure 1b shows a typical fluorescence intensity–time record when the microscope is zoomed into one of the bright spots shown in Figure 1a. The fluorescence intensity–time record is composed of sequential bursts of fluorescence photons separated by relatively longer dark periods. The observed fluorescence signals stem from the collisions and associations of NR molecules with the vesicle, while the dark periods correspond to the waiting times between successive associated events during which the NR molecules are in water and have undetectable fluorescence. The histogram of the fluorescence intensity–time record from the data of Figure 1b has two Gaussian peaks with the major peak centered at ~ 1 counts/ms, which corresponds to the distribution of the background signals during the dark periods. A less intense Gaussian peak located at a higher emission rate than the background signal arises from the emission of individual NR molecules colliding with the vesicle.^{14,15} The distribution is $\sim 10\%$ wider than that

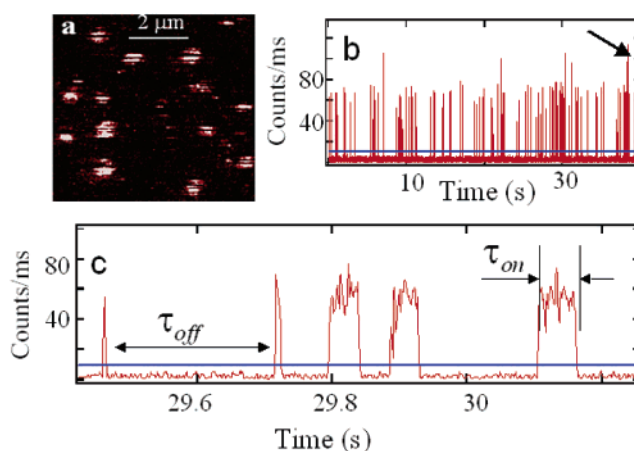


Figure 1. (a) Fluorescence image of surface immobilized lipid vesicles lit up by freely diffusing Nile Red molecules in solution. The dark stripes in the image are caused by fluorescence dark periods (off-times) occurring while the image is being scanned at 4 Hz/line. The Nile Red concentration in solution is 0.4 nM. (b) Fluorescence intensity recorded as function of time; the arrow points to a fluorescence burst formed by two Nile Red molecules visiting the vesicle simultaneously. (c) An expanded view of the intensity–time record shown in panel b; the straight line in panel c is the threshold, which corresponds to $\delta + 10\sqrt{\delta}$ (see details in the text) and is used to separate fluorescence signals from the background.

expected from Poisson statistics. The Gaussian center of the fluorescence emission rate distribution is proportional to the excitation power under our experimental conditions. Figure 1b shows there are a few (ca. 5 in this figure) fluorescence bursts with a significantly higher count rate than the average. Those high-intensity fluorescence bursts generally show a steplike character, as reported previously, and their average peak intensity is roughly twice the mean value of the dominant signal.¹⁵ This result suggests that they are generated by two NR molecules interacting with the same vesicle during the same burst period. At the low concentrations as used in Figure 1b and used in all subsequent experiments, there is only a small probability of observing simultaneous bursts from two molecules. The Gaussian profiled fluorescence count rate distribution has close to Poisson character. It arises because the detected molecules are confined in a relatively small volume, where both the excitation laser intensity and environment are approximately homogeneous.^{14,15,23,24} The data we present show that, by confining the target molecules in a volume much smaller than the focused laser beam, we can clearly tell how many target molecules exist in the probe volume from the detected fluorescence intensity.

The time period where the detected signals are above a specified threshold is τ_{on} and that during which the signals are below this threshold is τ_{off} (see Figure 1c). The association and dissociation reactions between freely diffusing NR molecules and the immobilized vesicle are characterized by the distribution functions of τ_{on} and τ_{off} which depend on the properties of NR and individual vesicles as well as the concentration and diffusion coefficient of NR and the vesicle size.¹⁵ The distribution of τ_{on} periods is influenced by both the natured residence kinetics of Nile Red in the vesicle and photobleaching. In the present experiments the contribution by photobleaching appears to be relatively small as shown below. At higher powers than used here, the occurrence of photobleaching becomes apparent and can significantly influence the on-times. We have observed previously that the $\langle \tau_{\text{off}} \rangle^{-1}$ (referred to as k_{off} hereafter) is proportional to the collision frequency of NR molecules with vesicles. The overall kinetics of the reactions of NR molecules

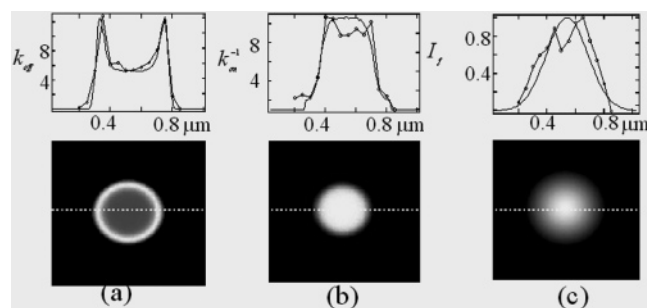


Figure 2. (Top panel) Lines with circles: simultaneously recorded k_{off} (a, in units of Hz), k_{on}^{-1} (b, in unit of ms), and fluorescence intensity (c) during the raster scanning of a vesicle through a focused laser beam. (Bottom panel) Simulated k_{off} (a), k_{on}^{-1} (b), and fluorescence intensity (c) images when scanning a circular disk through the laser focus. The sections along the dashed line in the images are also shown in the top panels as solid lines. The parameters used in simulation are the following: The $1/e^2$ width of laser focus is 580 nm. The scan step is 10 nm. The threshold is 10 (in unit of counts/ms), which corresponds to $\delta + 10\sqrt{\delta}$. The radius of circular disk was 50 nm. $M = 50$ counts/ms and $\sigma = 5$ count/ms. The off-time distribution was chosen as $(Ae^{-t/\tau_1} + Be^{-t/\tau_2})$ with $\tau_1 = 200$ ms, $A = 0.9$ and with $\tau_2 = 2$ ms, $B = 0.1$. The on-time distribution was chosen as $e^{-t/\tau_{\text{on}}}$ with $\tau_{\text{on}} = 10$ ms.

with a single vesicle is contained in the time autocorrelation function of the fluorescence intensity time record.¹⁵

In TTDOM, fluorescence intensity–time records are obtained at each pixel during a raster scan and then k_{off} and $\langle\tau_{\text{on}}\rangle$ (referred to as k_{on}^{-1} hereafter) are computed. When the signals are all below the threshold, both k_{off} and k_{on}^{-1} are defined as $1/T$ for convenience, where T here is the total number of data points in the record. The top panel of Figure 2 shows typical, simultaneously obtained variations of k_{off} , k_{on}^{-1} , and fluorescence intensity I_f when one vesicle is scanned through the laser focus. Such a scan can be accomplished within ~ 1 min, although longer signal collection times improve the signal-to-noise. As expected, the experimental, noisy intensity trace is determined by the profile of the focused laser beam. The experimental k_{off} and k_{on}^{-1} traces both have sharper edges than the intensity profile. A notable difference between the k_{off} and k_{on}^{-1} traces is that k_{off} has a nearly flat center area flanked by two sharp peaks at the edges, while the k_{on}^{-1} trace is more rectangular. The roughly flat signals in the center of the k_{on}^{-1} scan indicate that the excitation power does not significantly affect the k_{on}^{-1} signals under the present experimental conditions. If k_{on}^{-1} involved significant photobleaching, a noticeable dip should appear in the center of the scan because of the higher power in the center of the laser focus than at its edge. The signal magnitude in the center flat area of the k_{off} trace is determined by the rate at which freely diffusing NR molecules collide with the vesicle to produce a fluorescent state.^{14,15} The height in the center of the k_{on}^{-1} trace is the mean association time that is related to the details of the interaction of NR with the vesicle. The values of k_{on}^{-1} obtained from different lipid molecules were found to be significantly different.¹⁵

Simulations. Numerical simulations were carried out to explore the properties of k_{off} and k_{on}^{-1} images. Time trajectories were constructed from a model in which an immobilized planar object (for example, a circular disk with radius R , a square or a triangle with variable size or number of such objects) is targeted by spheres having negligible radius. Each hit is specified by a pseudorandom number chosen from a distribution function of time intervals between hits and a random choice of the

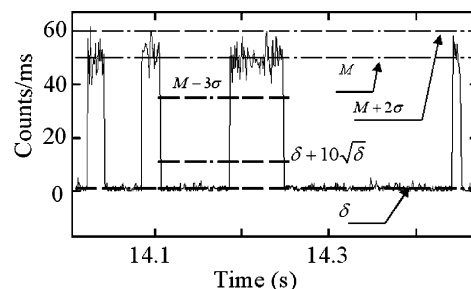


Figure 3. Part of a simulated trajectory and definitions. The Poisson noise has mean δ ; the burst height is M ; and the Gaussian noise associated with the burst has zero mean and a standard deviation of σ .

coordinates of the hit on the object plane. Each hit is assumed to generate a signal (mimicking the fluorescence) with a magnitude that varies with the planar coordinates according to a two-dimensional Gaussian distribution whose center location could be varied to mimic the scanning of a laser beam over the sample. The Gaussian parameters were chosen to reproduce the intensity point spread function when the object size was very small. Following each hit the signal was allowed to persist for a duration, the on-time period, chosen from pseudorandom numbers following a specific distribution function of on-times. The distribution functions were chosen from experiments:¹⁵ an exponential for the on-times and a double exponential for the off-times. The simulated intensity–time record, which is assigned to have bright periods corresponding to the objects being fluorescent followed by dark periods where there is no fluorescence from the object, was used to find values for k_{off} and k_{on}^{-1} for each chosen center location of the Gaussian. In this way a two-dimensional image was constructed. Noise was added to the signal trajectory by adding a Poisson distributed background signal with mean of δ to the dark periods and adding a Gaussian distributed noise to the fluorescent on-times. The Gaussian distribution noise is assigned to have zero mean and the standard deviation of σ when the magnitude of the burst is M , which is achieved when the object is located in the center of the two-dimensional Gaussian distribution that mimics the focused laser intensity distribution. Both M and σ vary with the planar coordinates according to the two-dimensional Gaussian distribution. Figure 3 shows part of a simulated trajectory with $M = 50$, $\sigma = 5$, and $\delta = 1$. The simulation generates intensity–time records that have the same characteristics as the experiments when the observed parameters are used in simulation.

The bottom panels in Figure 2 shows simulated k_{off} , k_{on}^{-1} , and fluorescence intensity images of a circular disk with a radius of 50 nm. The sections along the dashed lines through the images are overlapped with the corresponding experimental k_{off} , k_{on}^{-1} , and intensity curves, in the top panels of Figure 2. The k_{off} and k_{on}^{-1} images are much sharper at the edges than the intensity image. The simulated k_{off} image has peaks at the edges and dips to a flat area in the center having the magnitude of the mean collision rate. The k_{on}^{-1} image is flatter than the corresponding k_{off} image with a magnitude in the center equal to the mean duration of the hits. The sections of the images, equivalent to raster scans, are consistent with the corresponding experimental results as shown in the top panels in Figure 2.

Effect of Thresholds and Rapid Signal Fluctuations. The apparent size of an object in the images is primarily determined by both the focus spot of the laser beam and the thresholds used to separate the signals from the background. A high threshold can significantly reduce the widths of the traces, as

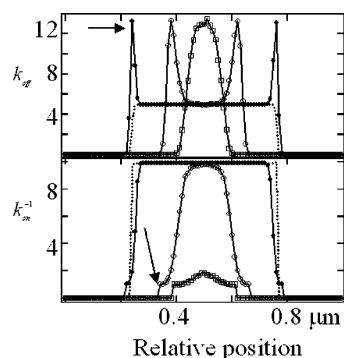


Figure 4. Simulated k_{off} (top) and k_{on}^{-1} (bottom) scans obtained by using thresholds of 10 (filled circles), 35 (open circles), and 50 (squares). The radius of disk was 10 nm; the other parameters are as listed in Figure 2. The dashed curves are simulated k_{off} and k_{on}^{-1} traces obtained with a threshold of 10 and without the rapid fluorescence fluctuations. Two arrows in the figure point to a sharp peak and a shoulder that are caused by rapid fluorescence fluctuations.

shown in Figure 4. However, when a threshold larger than $M - 3\sigma$ is applied, the signals in the center of the images start to deviate from the corresponding intrinsic collision rate and the mean of the on-times. To obtain the correct collision rate and fluorescence on-times, a threshold smaller than $M - 3\sigma$ must be used. In practice, a threshold as low as $\delta + 10\sqrt{\delta}$ (see Figures 1c and 3) can be applied to data sets. With thresholds between $\delta + 10\sqrt{\delta}$ and $M - 3\sigma$, the intrinsic collision rate and the mean of the fluorescence on-times can be accurately recovered. From the experimental data shown in the top panel of Figure 2, k_{off} is measured to be ~ 5 Hz, and k_{on}^{-1} is ~ 10 ms. The experimental parameters were $N = 1.2 \times 10^{11} \text{ cm}^{-3}$ (0.2 nM) and with $D = 1.2 \cdot 10^{-6} \text{ cm}^2 \text{ s}^{-1}$,¹⁵ and assuming the vesicle has hemispherical shape and that each collision of NR molecules with the vesicle generates a detectable fluorescence burst, the radius of the vesicle is estimated to be 55 nm. The simulations in Figure 4 also show how fluctuations in fluorescence signals (shown in Figures 1c and 3 as rapid signal fluctuations within individual bursts) can affect the k_{off} and k_{on}^{-1} traces. By keeping the signals constant within the individual bursts, the two sharp peaks in the k_{off} trace and the two shoulders in the k_{on}^{-1} trace vanish. It follows that those peaks and shoulders are caused by the fluorescence fluctuations during the on-times. The effect of those rapid signal fluctuations also depends on the thresholds. As shown in Figure 4, when thresholds between $\delta + 10\sqrt{\delta}$ and $M - 3\sigma$ are applied, the rapid fluorescence fluctuations contribute to the k_{off} and k_{on}^{-1} by introducing some small off-times and on-times into the statistics when the object is located at the edge of the laser focus, where the excitation power is lower. Moving the object into the center of the laser focus increases the effective excitation power and increases the fluorescence signals. Ultimately all the bursts will be above the threshold, and the rapid fluctuations no longer contribute to the k_{off} and k_{on}^{-1} traces, then, the signals are completely determined by the intrinsic collision rate and the mean on-times. When a threshold of M or greater is applied, both k_{off} and k_{on}^{-1} are dominated by the rapid fluorescence fluctuations, and the intrinsic mean off-time and mean on-times have little effect on the k_{off} and k_{on}^{-1} traces. When the threshold falls between $M - 3\sigma$ and M , the k_{off} trace still has two peaks flanking a flat center area, but the magnitude in the center is determined by both the intrinsic mean of off-times and the frequency of the rapid signal fluctuations; under these conditions the k_{on}^{-1} trace shows a peak with two shoulders and

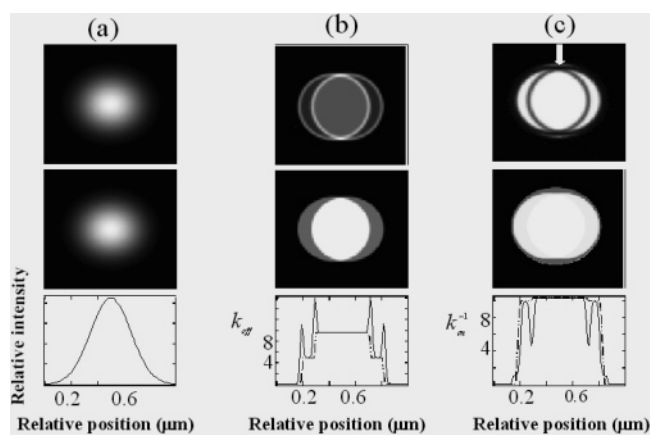


Figure 5. Simulated fluorescence intensity (a), k_{off} (b), and k_{on}^{-1} (c) images of two circular disks of radius of 10 nm separated by 100 nm obtained with (top panel) and without (center) the rapid fluorescence fluctuations. The corresponding median cross sections are shown in the bottom panel as the solid curves (with fluctuations) and the overlapped dashed curves (without). The other parameters are as listed in Figure 2. The arrow on the top of the k_{on}^{-1} image points to one of the lobes caused by the co-visiting.

a magnitude determined by the intrinsic mean of on-time and the durations of the rapid fluctuations.

Effect of Rapid Signal Fluctuations on Images of Pairs of Objects. The physical origins of the rapid fluorescence fluctuations have not yet been fully elucidated. They probably involve not only the laser intensity fluctuations but also rapid changes of environment surrounding individual NR molecules, which could cause fluctuations in the absorption and fluorescence spectra, quantum yields, and orientational motions of NR. It is also possible that there are fluctuations caused by intersystem crossing to triplet states.^{25–27} Those rapid signal fluctuations that cause the sharp peaks and shoulders do not interfere with the high-resolution imaging as demonstrated in Figure 5, which shows the simulated k_{off} , k_{on}^{-1} , and intensity images of two objects with and without them. The intensity images of the pair of objects in Figure 5 show only one peak. However, the simulated k_{off} and k_{on}^{-1} images based on intensity–time records with rapid signal fluctuations show that there are two objects whose separation is 100 nm. The corresponding collision rates and hence the sizes of the two objects can be measured directly from the k_{off} image, while the k_{on}^{-1} image provides the corresponding mean of on-times for each of the objects.¹⁵ The observed sharp bright rings in the k_{off} image and the sharp dim rings in the k_{on}^{-1} image are caused by the rapid fluorescence signal fluctuations, demonstrated by the fact that they disappear when the fluctuations are removed from the simulation, as shown in the center panel of Figure 5. When the signal fluctuations are shut off, the simulated k_{off} image still shows two objects, but the k_{on}^{-1} image does not clearly resolve them. In the simulations of Figure 5, the two objects have the same collision rates and mean on-times. When both objects are in the center of the laser focus the collision rate is doubled. This effect gives rise to the two-step feature in the k_{off} image and its sections. When two objects having the same k_{on}^{-1} are in the laser focus, the value of k_{on}^{-1} for the pair is the same as that for each object when there is no co-visiting. If the two objects have different k_{on}^{-1} , the k_{on}^{-1} will be different from either of the means. The larger is the difference between the two k_{on}^{-1} values, the higher is the contrast in k_{on}^{-1} image. The k_{on}^{-1} images obtained from intensity–time records with rapid signal

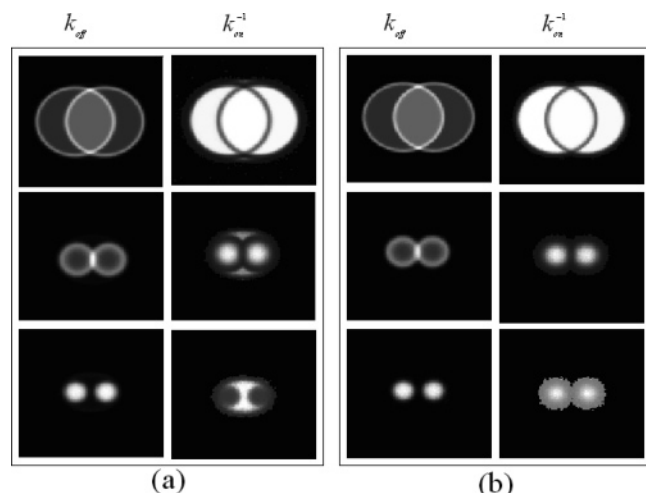


Figure 6. Simulated k_{off} (left in each panel) and k_{on}^{-1} (right in each panel) images of two circular disks of radius 10 nm separated by 200 nm obtained with a threshold of 10 (top), 40 (center), and 50 (bottom): (a) with co-visiting events (see text for details) and (b) without co-visiting events. The other parameters are as listed in Figure 2.

fluctuations have a resolution that is not limited by the on-times. Fortunately, the rapid signal fluctuations are inherent characteristics of single molecule fluorescence signals. It should be noted that the k_{off} and k_{on}^{-1} images shown in the top panel of Figure 5 actually are identical with the corresponding k_{off} and k_{on}^{-1} images shown in the center panel after the sharp bright and dim rings are removed from the corresponding images.

Effect of Co-visitation on Images of Pairs of Objects Obtained with Different Thresholds. The signals in the center of the k_{on}^{-1} traces in Figure 5 are a little higher than signals at the edges. This effect is caused by two or more probes visiting the object during a single on-period and results in overlapping bursts that increase the on-times. These co-visiting events are rare at our experimental concentrations but are observable. Two or more molecules visiting a vesicle simultaneously have been observed previously.^{14,15} One of the fluorescence bursts generated by two molecules visiting a vesicle simultaneously is pointed out in Figure 1b. Lowering the concentration of beacons reduces the probability of those events. The other features caused by the co-visiting events are the two lobes flanking the k_{on}^{-1} image, one of which is identified by the arrow in Figure 5c. These lobes and the subtle increase in the center of the k_{on}^{-1} images in Figure 5 both disappear when the co-visiting events are excluded in the simulation, as shown in Figure 6. Those co-visiting events contribute to k_{on}^{-1} signals only when both objects are located in the lobe of the laser focus, which explains why there is no lobe in either left or right sides of the k_{on}^{-1} image.

Figure 6 shows two panels (a and b), each consisting of three sets of images obtained with different thresholds. The images in the (a) panel were based on the model described above for immobilized objects visited by beacons independently, so there are co-visiting events. Co-visiting was excluded in the images in panel b. Comparing images in those two panels, we find that co-visiting affects only the k_{on}^{-1} images. Figure 6 also shows the effect of threshold on the images of two objects. With the threshold of $\delta + 10\sqrt{\delta}$ (top panels), the image sizes of individual objects are relatively large and they overlap. With the threshold of $M - 2\sigma$, the image sizes and the overlap of individual objects are reduced significantly. The k_{on}^{-1} image

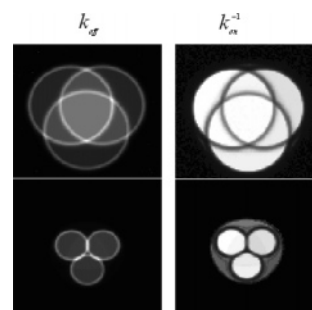


Figure 7. Simulated k_{off} and k_{on}^{-1} images of three circular disks of radius 10 nm with separations of 200 nm arranged in an equilateral triangle obtained with a threshold of 10 (top panel) and 40 (bottom). The other parameters are as listed in Figure 2.

shows two separate objects in the absence of co-visiting. Increasing the threshold further to M (bottom panels) results in two separated objects except for the k_{on}^{-1} image with co-visiting, which shows two dim disks surrounded partially by two bright and overlapping lobes. With the threshold of M , the k_{off} image is dominated by the rapid signal fluctuations, while the k_{on}^{-1} image is determined by both rapid signal fluctuations and the two co-visitation lobes. All the k_{on}^{-1} images in the (a) panel are identical with those corresponding k_{on}^{-1} images in the (b) panel of Figure 6 when co-visiting is excluded. Increasing the threshold further above M reduces the apparent size of an object in the k_{off} image more effectively than in the k_{on}^{-1} image as evident from data in Figures 4 and 6. This is because the threshold has a different effect on the image size of an object in the k_{off} and k_{on}^{-1} images. When thresholds that are equal to or larger than $M + 4\sigma$ are applied, the probability of observing single beacon signals is less than 0.03%. In that case, the k_{off} and k_{on}^{-1} signals are dominated by the co-visiting events, the frequency and the duration of which can be estimated from the traces.

Images of More Complex Structures. A high threshold reduces the apparent size of an object and clarifies the images as illustrated in Figure 7. The top panel shows the images of three circles at vertices of a triangle with a side of 200 nm, which are more clearly resolved in the bottom panel obtained with the increased threshold.

We have also simulated images from objects having different shapes. The simulations for a square and a triangle are shown in Figure 8. The results in Figure 8 clearly show that TTDOM can distinguish the shapes that could not be resolved by a conventional optical microscope.

Comparison of Simulations with Experiments. The experimental method of vesicle preparation described above is aimed at generating surface adsorbed vesicles separated by more than the confocal spot size. The mean vesicle size is predetermined by the membrane pore diameter, in this case 100 nm, but the actual sizes, shapes, and states of aggregation are not determined by confocal microscopy. However, these conditions enable the observation of properties of one vesicle at a time as is evident from the TTDOM traces typified by Figure 2. To prepare surface adsorbed vesicle aggregates, we first gradually deposited a large number of vesicles on the glass surface so that $\sim 50\%$ percent of the surface area was covered by vesicles. Then some vesicles were removed by washing with buffer solution. This procedure created a surface where 90% of the TTDOM traces are similar to those shown in Figure 2, but $\sim 10\%$ of them are clearly not single vesicle traces but are similar to the simulated TTDOM traces for a pair of particles.

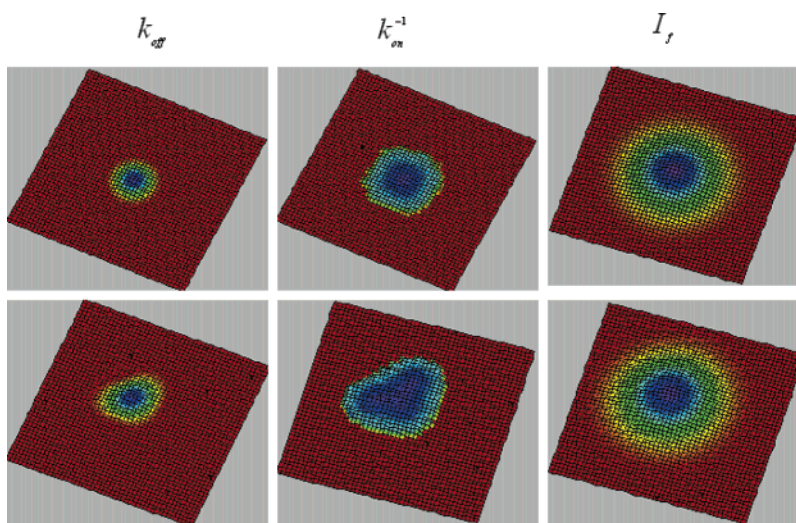


Figure 8. Simulated k_{off} , k_{on}^{-1} , and intensity images of a square of side 100 nm (top) and a 200 nm \times 200 nm \times 282 nm triangle (bottom) obtained with a threshold of 40. The other parameters are as listed in Figure 2.

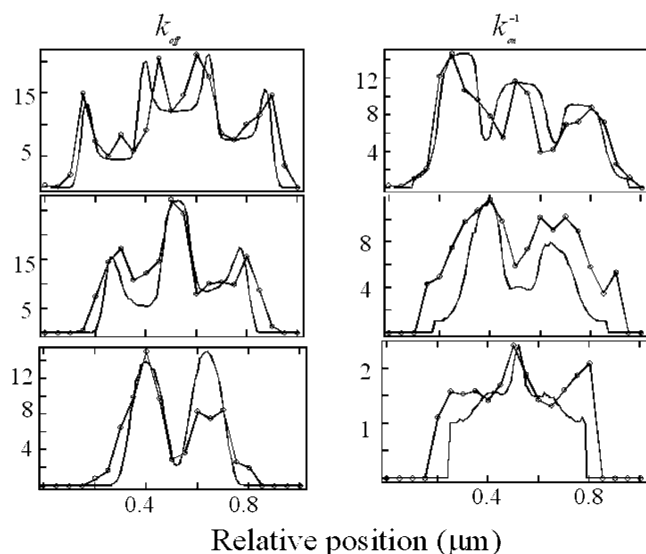


Figure 9. Experimental (curves with circles) and simulated k_{off} and k_{on}^{-1} traces obtained with thresholds of $S + 10\delta$, $M - 2\sigma$, and $M + 2\sigma$. The experimental thresholds and experimentally measured parameters (see details in the text) were used in the corresponding simulations. The other parameters are as listed in Figure 2.

We have shown one of these in our previous report¹⁴ and Figure 9 shows another example. The manner by which these traces vary with threshold shows up the basic shape of the underlying aggregate of vesicles.

Figure 9 shows experimental k_{off} and k_{on}^{-1} signals calculated by applying different thresholds to a series of experimental intensity–time records, which were recorded when a bright spot was scanned through the laser focus. The fluorescence intensity scan is a one-dimensional Gaussian in this case. The experimental values of k_{off} and k_{on}^{-1} at the threshold of $\delta + 10\sqrt{\delta}$ are consistent with the presence of two vesicles of radius ~ 44 and ~ 62 nm having mean association times of ~ 14 and ~ 10 ms. These parameters were then used to simulate a signal for two coplanar circular disks having an edge-to-edge separation of 130 nm. The simulated results reproduce the observations as shown in Figure 9. Clearly, two vesicles separated by 130 nm are being spatially resolved by this method. We have observed previously that the association time with vesicles depends on the properties of the vesicles, but is insensitive to

their size.¹⁵ Accordingly, the results in Figure 9 indicate that photophysics of NR molecules are not the same in the two vesicles.

From simulation, we have predicted that two point objects with a separation as small as 30 nm could be resolved. Important parameters which affect the resolution are the mean value and width of the fluorescence count rate distribution. Sharper edges in the k_{off} and k_{on}^{-1} traces are obtained at narrower count rate widths. As observed previously, the two peaks in the count rate distribution of a typical intensity–time record (Figure 1) are reasonably well separated. In simulations, we have seen that reducing the overlap between these two peaks results in sharper edges in the images and hence higher resolution. For a point object and a count rate distribution of zero width, the k_{off} and k_{on}^{-1} curves would become vertical to the baseline at both edges, in which case, two objects separated by any distance would be distinguishable.

Conclusion and Outlook

We have demonstrated experimentally and also by simulations that optical microscopy beyond the diffraction limit can be accomplished by an approach that records the fluorescence off-rate and the mean of fluorescence on-times of freely diffusing molecular beacons colliding with objects of interest. While initial experimental results and simulations prove the potential of this new microscopy, many improvements are needed. For example, standard samples are needed to calibrate distance measurements. Fluorescent spheres are often used as standard samples to calibrate and align the confocal optical microscope. TTDOM requires nanometer rulers rather than fluorescent spheres. Those nanorulers could be pairs or groups of hydrophobic structures with variable size, shape, and separation between them. We have observed pairs of vesicles prepared by the method described above and shown in Figure 9, but that approach does not prepare pairs of vesicles with specific separations.

The future applications of TTDOM will also depend on the development of appropriate environmentally sensitive beacons including organic molecules and quantum dots (QDs). Examples include the pH-sensitive dye Carboxy SNARF-1^{28,29} that changes quantum yield when the local pH changes and the dielectric and viscosity sensitive dye DCDHFs whose quantum yield varies as a function of solvent and solvent viscosity.³⁰ Both SNARF-1 and DCDHFs have been characterized and used

in single molecule experiments.^{28–30} The FLAsH-type dyes, which have a 50 times increase in fluorescence when they bind to a particular peptide sequence,³¹ and probes that emit strongly only when both H⁺ and Na⁺ exist nearby³² are other candidates. Compared with fluorescent dyes, QDs have several advantageous properties, such as extreme brightness, high resistance to photobleaching, high molar extinction coefficients (~10–100 times that of organic dyes), and broad adsorption with narrow, symmetric photoluminescence spectra.³³ Those properties are enabling the use of QDs in biological and medical areas.³⁴ While the fluorescence intermittency^{35–38} of QDs imposes some limitations in their applications in conventional fluorescence imaging,³⁹ it also opens an opportunity of use of QDs as fluorescent probes in TTDOM for high-resolution fluorescence off-rate and fluorescence on-time imaging. QDs that are closer than the diffraction limit have been discriminated by their emitted intensity and blinking behavior.⁴⁰

Acknowledgment. This work was supported by NIH grants GM48130 and RFA-RM-04-001, using instrumentation developed by the NIH Research Resource grant NIH P41 RR001348.

References and Notes

- (1) Born, M.; Wolf, E. *Principles of Optics*, 5th ed.; Pergamon Press: New York, 1975.
- (2) Pohl, D. W. Scanning Near-field Optical Microscopy (SNOM). In *Advances in Optical and Electron Microscopy*; Sheppard, T. M., Ed.; Academic Press: London, UK, 1990; pp 243–312.
- (3) Betzig, E.; Isaacson, M.; Lewis, A. *Appl. Phys. Lett.* **1987**, *51*, 2088–2090.
- (4) Higgins, D.; Mei, E. Near-Field Scanning Optical Microscopy. In *Scanning Probe Microscopy and Spectroscopy, Theory, Techniques, and Applications*, 2nd ed.; Bonnell, D., Ed.; Wiley-VCH: New York, 2001; p 371.
- (5) Paesler, M. A.; Moyer, P. J. *Near Field Optics, Theory, Instrumentation, and Applications*; Wiley: New York, 1996.
- (6) Hanninen, P. E.; Hell, S. W.; Salo, J.; Soini, E.; Cremer, C. *Appl. Phys. Lett.* **1995**, *66*, 1698–1700.
- (7) Klar, T. A.; Jakobs, S.; Dyba, M.; Egner, A.; Hell, S. W. *Proc. Natl. Acad. Sci. U.S.A.* **2000**, *97*, 8206–8210.
- (8) Hofmann, M.; Eggeling, C.; Jakobs, S.; Hell, S. W. *Proc. Natl. Acad. Sci. U.S.A.* **2005**, *102*, 17565–17569.
- (9) Gordon, M. P.; Ha, T.; Selvin, P. R. *Proc. Natl. Acad. Sci. U.S.A.* **2004**, *101*, 6462–6465.
- (10) Qu, X.; Wu, D.; Mets, L.; Scherer, N. F. *Proc. Natl. Acad. Sci. U.S.A.* **2004**, *101*, 11298–11303.
- (11) Ram, S.; Ward, E. S.; Ober, R. J. *Proc. Natl. Acad. Sci. U.S.A.* **2006**, *103*, 4457–4462.
- (12) Michalet, X.; Weiss, S. *Proc. Natl. Acad. Sci. U.S.A.* **2006**, *103*, 4797–4798.
- (13) Fang, N.; Lee, H.; Sun, C.; Zhang, X. *Science (Washington, DC)* **2005**, *308*, 534–537.
- (14) Mei, E.; Gao, F.; Hochstrasser, R. M. *Phys. Chem. Chem. Phys.* **2006**, *8*, 2077–2082.
- (15) Gao, F.; Mei, E.; Lim, M.; Hochstrasser, R. M. *J. Am. Chem. Soc.* **2006**, *128*, 4814–4822.
- (16) Bopp, M. A.; Sytnik, A.; Howard, T. D.; Cogdell, R. J.; Hochstrasser, R. M. *Proc. Natl. Acad. Sci. U.S.A.* **1999**, *96*, 11271–11276.
- (17) Johnson, J. M.; Ha, T.; Chu, S.; Boxer, S. G. *Biophys. J.* **2002**, *83*, 3371–3379.
- (18) Feng, Z. V.; Spurlin, T. A.; Gewirth, A. A. *Biophys. J.* **2005**, *88*, 2154–2164.
- (19) Enders, O.; Ngezahayo, A.; Wiechmann, M.; Leisten, F.; Kolb, H. A. *Biophys. J.* **2004**, *87*, 2522–2531.
- (20) Schönherr, H.; Johnson, J. M.; Lenz, P.; Frank, C. W.; Boxer, S. G. *Langmuir* **2004**, *20*, 11600–11606.
- (21) Reviakine, I.; Brisson, A. *Langmuir* **2000**, *16*, 1806–1815.
- (22) Jin, A. J.; Edidin, M.; Nossal, R.; Gershfeld, N. L. *Biochemistry* **1999**, *38*, 13275–13278.
- (23) Eigen, M.; Rigler, R. *Proc. Natl. Acad. Sci. U.S.A.* **1994**, *91*, 5740–5747.
- (24) Chen, Y.; Muller, J. D.; So, P. T. C.; Gratton, E. *Biophys. J.* **1999**, *77*, 553–567.
- (25) Mei, E.; Vinogradov, S.; Hochstrasser, R. M. *J. Am. Chem. Soc.* **2003**, *125*, 13198–13204.
- (26) Lu, H. P.; Xie, X. S. *Nature* **1997**, *385*, 143–146.
- (27) Yip, W.-T.; Hu, D.; Yu, J.; Vanden, Bout, D. A.; Barbara, P. F. *J. Phys. Chem. A* **1998**, *102*, 7564–7575.
- (28) Fu, Y.; Collinson, M. M.; Higgins, D. A. *J. Am. Chem. Soc.* **2004**, *126*, 13838–13844.
- (29) Brasselet, S.; Moerner, W. E. *Single Mol.* **2000**, *1*, 17–23.
- (30) Willets, K. A.; Callis, P. R.; Moerner, W. E. *J. Phys. Chem. B* **2004**, *108*, 10465–10473.
- (31) Adams, S. R.; Campbell, R. E.; Gross, L. A.; Martin, B. R.; Walkup, G. K.; Yao, Y.; Llopis, J.; Tsien, R. Y. *J. Am. Chem. Soc.* **2002**, *124*, 6063–6076.
- (32) Uchiyama, S.; McClean, G., D.; Iwai, K.; Silva, A. P. d. *J. Am. Chem. Soc.* **2005**, *127*, 8920–8921.
- (33) Medintz, I. L.; Uyeda, H. T.; Goldman, E. R.; Mattoussi, H. *Nat. Mater.* **2005**, *4*, 435–446.
- (34) Alivisatos, A. P.; Gu, W.; Larabell, C. *Annu. Rev. Biomed. Eng.* **2005**, *7*, 55–76, 53 plates.
- (35) Nirmal, M.; Dabbousi, B. O.; Bawendi, M. G.; Macklin, J. J.; Trautman, J. K.; Harris, T. D.; Brus, L. E. *Nature* **1996**, *383*, 802–804.
- (36) Kuno, M.; Fromm, D. P.; Hamann, H. F.; Gallagher, A.; Nesbitt, D. J. *J. Chem. Phys.* **2000**, *112*, 3117–3120.
- (37) Hohng, S.; Ha, T. *J. Am. Chem. Soc.* **2004**, *126*, 1324–1325.
- (38) Yao, J.; Larson, D. R.; Vishwasrao, H. D.; Zipfel, W. R.; Webb, W. W. *Proc. Natl. Acad. Sci. U.S.A.* **2005**, *102*, 14284–14289.
- (39) Dahan, M.; Levi, S.; Luccardini, C.; Rostaing, P.; Riveau, B.; Triller, A. *Science* **2003**, *302*, 442–445.
- (40) Lidke, K. A.; Rieger, B.; Jovin, T., M.; Heintzmann, R. *Opt. Express* **2005**, *13*, 7052–7062.